

HD 76920 b pinned down: a detailed analysis of the most eccentric planetary system around an evolved star

C. Bergmann^{1,2*†}, M. I. Jones^{3,4}, J. Zhao^{1,5}, A. J. Mustill⁶, R. Brahm^{7,8}, P. Torres⁹, R. A. Wittenmyer¹⁰, F. Gunn¹¹, K. R. Pollard¹¹, A. Zapata⁹, L. Vanzi⁹, S. Wang¹²

¹Exoplanetary Science at UNSW, School of Physics, UNSW Sydney, NSW 2052, Australia

²Deutsches Zentrum für Luft- und Raumfahrt, Münchener Str. 20, 82234 Weßling, Germany

³European Southern Observatory, Alonso de Córdova 3107, Casilla 19001, Santiago, Chile

⁴Instituto de Astronomía, Universidad Católica del Norte, Angamos 0610, 1270709, Antofagasta, Chile

⁵Penn State University, Department of Astronomy and Astrophysics, University Park, PA 16802, USA

⁶Lund Observatory, Department of Astronomy & Theoretical Physics, Lund University, Box 43, 221 00 Lund, Sweden

⁷Millennium Institute for Astrophysics, Chile

⁸Facultad de Ingeniería y Ciencias, Universidad Adolfo Ibáñez, Av. Diagonal las Torres 2640, Peñalolén, Santiago, Chile

⁹Department of Electrical Engineering and Center of Astro Engineering, Pontificia Universidad Católica de Chile, Av. Vicuña Mackenna 4860, Santiago, Chile

¹⁰University of Southern Queensland, Centre for Astrophysics, Toowoomba, Queensland 4350, Australia

¹¹School of Physical and Chemical Sciences, Te Kura Matū, University of Canterbury, Christchurch 8020, New Zealand

¹²Department of Astronomy, Indiana University, Bloomington, IN 47405, USA

Abstract

We present 63 new multi-site radial velocity measurements of the K1III giant HD 76920, which was recently reported to host the most eccentric planet known to orbit an evolved star. We focussed our observational efforts on the time around the predicted periastron passage and achieved near-continuous phase coverage of the corresponding radial velocity peak. By combining our radial velocity measurements from four different instruments with previously published ones, we confirm the highly eccentric nature of the system, and find an even higher eccentricity of $e = 0.8782 \pm 0.0025$, an orbital period of $415.891^{+0.043}_{-0.039}$ d, and a minimum mass of $3.13^{+0.41}_{-0.43} M_J$ for the planet. The uncertainties in the orbital elements are greatly reduced, especially for the period and eccentricity. We also performed a detailed spectroscopic analysis to derive atmospheric stellar parameters, and thus the fundamental stellar parameters (M_* , R_* , L_*), taking into account the parallax from Gaia DR2, and independently determined the stellar mass and radius using asteroseismology. Intriguingly, at periastron the planet comes to within 2.4 stellar radii of its host star's surface. However, we find that the planet is not currently experiencing any significant orbital decay and will not be engulfed by the stellar envelope for at least another 50 – 80 Myr. Finally, while we calculate a relatively high transit probability of 16%, we did not detect a transit in the TESS photometry.

Keywords: planetary systems – stars: individual: HD 76920 – techniques: radial velocities

1 INTRODUCTION

Since the first detection of a planet around a main-sequence star more than two decades ago (Mayor & Queloz, 1995), thousands of planetary systems have been found with astonishing diversity. The transit method has produced the most planet discoveries to date, mostly due to the overwhelming success of NASA's *Kepler* mission (Borucki et al., 2010). Yet, a significant fraction of all planets has been found using the radial velocity

(RV) technique, including many longer-period planets, for which ground-based Doppler searches have a natural advantage over short-lived space missions. The RV method also remains a valuable tool for the detection and characterization of planets, as it yields the minimum mass of a planet and therefore nicely complements the transit method, which yields the size of a planet. Space-based transit searches such as *Kepler* (Borucki et al., 2010) or TESS (Ricker et al., 2015) also rely on ground-based RV follow-up observations to confirm their planet candidates, to determine their masses and hence densities, and to search for additional planets in these

*Visiting Astronomer, University of Canterbury Mt John Observatory

†E-mail: cbergmann001@gmail.com

systems.

Slowly rotating solar-type and late-type stars are ideal targets for Doppler planet searches, as their spectra exhibit numerous sharp absorption lines. However, main-sequence stars more massive than about $1.5 M_{\odot}$ are generally not suitable for precise RV measurements, due to their high temperatures and fast rotation rates (e.g. Galland et al., 2005). Consequently, the occurrence rate and distribution of planets as a function of stellar mass and metallicity for intermediate-mass stars are not as well-established compared to planets around lower-mass stars (e.g. Johnson et al., 2010; Reffert et al., 2015; Jones et al., 2016; Wittenmyer et al., 2017a). In order to learn more about planetary systems around these intermediate-mass stars, several planet search programmes have been specifically targeting evolved stars of the same mass (often dubbed 'retired A-stars'), as they do not suffer from these effects (e.g. Frink et al., 2002; Sato et al., 2003; Johnson et al., 2007; Niedzielski et al., 2007; Wittenmyer et al., 2011; Jones et al., 2011).

More than 100 planets have now been discovered orbiting giant stars, and except for the very few such systems discovered by *Kepler* (e.g. Quinn et al., 2015), all of these have been discovered via the RV technique. Notably the first planet found to orbit a giant star, ι Dra b, also happens to be on a very eccentric orbit with $e = 0.71$ (Frink et al., 2002; Kane et al., 2010). More recently, planets on even more eccentric orbits were found around the K3III giant BD+48 740 (HIP 12684) with $e = 0.76$ (Adamów et al., 2012, 2018), and around the K1III giant HD 76920 with $e = 0.86$ (Wittenmyer et al., 2017b). The latter currently claims the title of being the most eccentric planet orbiting an evolved star, and is the subject of this work.

Orbits with certain combinations of high eccentricities and longitudes of periastron produce RV curves that are essentially flat for the majority of the orbital period and only exhibit a narrow peak near periastron passage. However, because nearly all the information needed to determine the orbital parameters, including the RV semi-amplitude and thus the minimum mass of the planet, is contained in this short phase of the orbit, it is rather difficult from an observational point of view to obtain a good orbital solution for such systems. In their discovery paper, Wittenmyer et al. (2017b) pointed out that the periastron passage of HD 76920 b still needed better observational sampling in order to sufficiently constrain the orbital elements and minimum mass of the planet. We therefore planned a multi-site observing run and successfully filled in the gap in the phase coverage near periastron passage with RV measurements.

In this paper we present the results of our observational campaign. We describe our multi-site observations and RV measurements in Sections 2 and 3, respectively. We then present newly computed stellar parameters in Section 4. In Section 5 we describe the orbit fitting pro-

cess and present our improved orbital solution. We also present an upper mass limit for HD 76920 b in Section 6, followed by a discussion of our findings in Section 7.

2 OBSERVATIONS

Between January and March 2018, we acquired 63 observations of HD 76920 using four different instruments. Firstly, 39 were taken at the University of Canterbury Mt John Observatory (UCMJO) in Lake Tekapo, New Zealand, using the 1-m McLellan telescope in conjunction with the HERCULES spectrograph (Hearnshaw et al., 2002). Of these, 19 were taken with a 100- μ m core-diameter fibre ('fibre 1'), corresponding to a resolving power of $R \sim 41\,000$, and another 20 were taken with a different 100- μ m core-diameter fibre with a 50- μ m micro-slit attached to its end ('fibre 3'), corresponding to a resolving power of $R \sim 70\,000$. These observations are referred to below as MJ1 and MJ3, respectively.

A further 8 observations were obtained with the CHIRON spectrograph (Tokovinin et al., 2013) attached to the 1.5-m telescope at Cerro Tololo Inter-American Observatory (CTIO) in Chile. These new spectra were obtained using the 'slit mode', which delivers a resolving power of $R \sim 95\,000$ and a total system efficiency of $\sim 2\%$. Both HERCULES and CHIRON employ the iodine-cell technique (e.g. Butler et al., 1996; Endl et al., 2000), i.e. during the observations a gas absorption cell containing molecular iodine (kept at a constant temperature of $50.0 \pm 0.1^{\circ}\text{C}$) is placed in the light path for wavelength calibration and for modelling of the instrumental profile.

Finally, we also obtained 15 spectra using FIDEOS (Vanzi et al., 2018) and one new spectrum using FEROS (Kaufer et al., 1999). These two high-resolution ($R \sim 43\,000$ and $R \sim 48\,000$, respectively) spectrographs are located at La Silla Observatory in Chile, and are attached to the ESO 1-m and 2.2-m telescopes, respectively. In addition, they are both fed by multiple optical fibres, allowing a simultaneous ThAr wavelength calibration during the science exposure for precision radial velocities.

3 RADIAL VELOCITIES

Raw-reduction of the HERCULES observations was performed with the latest version (v5.2.9) of the HERCULES Reduction Software Package (HRSP; Skuljan, 2004) and the pipeline described in Bergmann (2015). From the reduced spectra we derived radial velocities using our version of the AUSTRAL Doppler code described by Endl et al. (2000). We used a high-S/N, iodine-free spectrum of the K1III star ν Octantis as a template (Ramm et al., 2016). While this setup has proven to deliver long-term RV precisions of about 4.5 m s^{-1} (with short-term precision of $\lesssim 3 \text{ m s}^{-1}$) for bright solar-type stars (Bergmann, 2015; Bergmann et al., 2015), the

fainter magnitude of HD 76920 ($V = 7.8$) combined with poor seeing conditions for a majority of the nights resulted in single-shot uncertainties of typically 14.5 m s^{-1} for the higher-resolution fibre, and 16.5 m s^{-1} for the lower-resolution fibre, which was preferred if the seeing was worse than about 3 arcsec.

The CHIRON spectra were reduced with the observatory customized pipeline, which provides order by order extracted and wavelength calibrated spectra for CHIRON users. The RVs were computed following the method described in Jones et al. (2017). We note that the new CHIRON velocities have larger uncertainties compared to those in Wittenmyer et al. (2017b), as the new spectra were obtained in ‘slit mode’, rather than in ‘fibre-slicer mode’ ($R \sim 80000$). As a consequence, although the new data were taken at a slightly higher resolving power, the efficiency is drastically reduced (by a factor of ~ 3), when compared to ‘fibre-slicer mode’, directly translating into lower S/N data, and thus leading to larger RV uncertainties. We have also recomputed the ‘fibre-slicer mode’ CHIRON RVs published in Wittenmyer et al. (2017b), including the new data, which resulted in small but non-negligible changes.

Finally, both FIDEOS and FEROS data were processed with the CERES code (Brahm et al., 2017a), including a re-reduction of the 8 FEROS observations published in Wittenmyer et al. (2017b). CERES performs a standard échelle spectra reduction including bias subtraction, order tracing, optimal extraction, and wavelength calibration. The RVs for the two instruments were obtained from the cross-correlation function (CCF; Tonry & Davis, 1979). In the case of FIDEOS, the template used for the CCF corresponds to a numerical binary mask as explained in Brahm et al. (2017a), while in the case of FEROS data we use a high S/N template, which is built by stacking all of the individual observed spectra (Jones et al., 2017). The final velocities are obtained after correcting for the night drift (from the simultaneous calibration fibre) and barycentric velocity. Note that the newly computed FEROS RVs are superior to those presented in Wittenmyer et al. (2017b), where a much lower S/N template was used. All radial velocities used in this work and their corresponding uncertainties are summarized in Table 5.

4 STELLAR PARAMETERS

4.1 Spectroscopy

We computed the atmospheric parameters of HD 76920 using the ZASPE code (Brahm et al., 2017b). For this purpose, we first combined all of the individual FEROS spectra. The co-added master spectrum is then compared to the ATLAS9 grid of stellar models (Castelli & Kurucz, 2004), in carefully selected regions that are more sensitive to changes in the atmospheric parameters. This

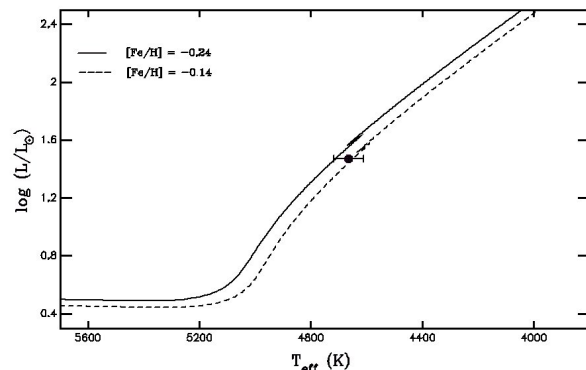


Figure 1. HR diagram showing the position of HD 76920. The solid and dashed lines correspond to PARSEC models with $M_{\star} = 1.0 M_{\odot}$, for $[\text{Fe}/\text{H}] = -0.24$ and -0.14 dex, respectively.

procedure is performed iteratively until we obtain the effective temperature (T_{eff}), the surface gravity ($\log g$), the stellar metallicity ($[\text{Fe}/\text{H}]$), and the projected rotational velocity ($v \sin i$). Using these derived parameters, we then computed the corresponding spectral energy distribution (SED). For this we used the BT-Settl-CIFIST models (Baraffe et al., 2015). From the SED we computed synthetic magnitudes and we compared them to the observed ones, which are listed in Table 1. During this process the stellar radius (R_{\star}) and the visual extinction (A_V) are derived, and thus the stellar luminosity (L_{\star}).

Finally, to obtain the stellar mass and evolutionary status of HD 76920, we compared the derived atmospheric parameters to the PARSEC evolutionary models (Bressan et al., 2012). We found that HD 76920 has a mass of $M_{\star} = 1.0 \pm 0.2 M_{\odot}$, and that it is ascending the red giant branch (RGB) phase. Figure 1 shows the position of HD 76920 in the HR diagram. For comparison, two different PARSEC isomass evolutionary tracks are overplotted. As can be seen, HD 76920 is located midway on its RGB ascent, and is reaching the luminosity bump region. We note that no horizontal branch track (i.e. Helium burning core) crosses its position in the HR diagram. All derived atmospheric and physical parameters are listed in Table 1.

4.2 Asteroseismology

As an independent method, we used asteroseismology to derive the stellar mass from the TESS (Ricker et al., 2015) photometric data. The TESS mission observed HD 76920 in the long cadence mode (30 min) in sectors 9, 10, and 11, adding up to a total of 3492 individual photometric measurements. To obtain the light curve we used the python tool `tesseract` (Rojas et al. in prep) using the `autoap` aperture. We removed the most deviant outliers using the `clean.py` tool and

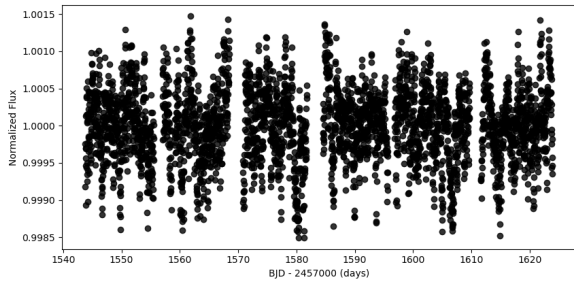


Figure 2. Normalized and detrended TESS photometry of HD 76920.

normalized each sector data independently by its median value. We also detrended the light curve using a linear fit, achieving a dispersion of 494.6 ppm. Figure 2 shows the resulting normalized TESS photometry of HD 76920. Then we ran a generalized Lomb-Scargle (GLS, Zechmeister & Kürster (2009)) routine to obtain the power spectral density (PSD) and search for asteroseismic power excess in order to measure ν_{\max} and $\Delta\nu$. We also corrected the background using a very wide gaussian profile kernel. After this correction we followed the method presented in Jones et al. (2018), which consists of convolving a gaussian profile with a $\sigma = 12\mu\text{Hz}$ kernel around the power excess in order to find the peak that corresponds to ν_{\max} . To obtain $\Delta\nu$ we convolved a gaussian profile with a $\sigma = 1\mu\text{Hz}$ kernel and we ran an autocorrelation routine. Using this procedure, we obtained $\nu_{\max} = 54.01 \pm 2.75 \mu\text{Hz}$ and $\Delta\nu = 5.64 \pm 0.24 \mu\text{Hz}$. From these values, and following the scaling relations presented in Kjeldsen & Bedding (1995), we obtained a mass of $M_{\star} = 1.29 \pm 0.17 M_{\odot}$ and a radius $R_{\star} = 9.07 \pm 0.63 R_{\odot}$. The corresponding $1\text{-}\sigma$ error bars were obtained from a bootstrap analysis. The asteroseismic mass and radius are in reasonably good agreement with the spectroscopic values.

5 ORBITAL SOLUTION

Wittenmyer et al. (2017b) published 37 RVs of HD 76920 obtained with three different spectrographs. Of these, 17 were taken with UCLES (Diego et al., 1990) installed at the 3.9-m Anglo-Australian Telescope (AAT), 12 were taken with CHIRON at the 1.5-m telescope at CTIO, and 8 were taken with FEROS installed at the 2.2-m telescope at La Silla.

We combined our 63 new RV measurements with the 12 re-reduced CHIRON RVs, the 8 newly reduced FEROS RVs, and the remaining 17 UCLES RVs from Wittenmyer et al. (2017b), and fitted a single Keplerian model to the combined data set consisting of a total of 100 RVs. We used the `emcee` 2.2.1 package (Foreman-Mackey et al., 2013), a pure-python implementation of the Affine-Invariant Markov chain Monte Carlo (MCMC)

Table 1 Stellar parameters of HD 76920

Parameter	Value	Method/Source
B [mag]	8.83 ± 0.02	Tycho-2
V [mag]	7.82 ± 0.01	Tycho-2
G [mag]	7.5144 ± 0.0003	Gaia
J [mag]	5.95 ± 0.02	2MASS
H [mag]	5.41 ± 0.04	2MASS
K [mag]	5.25 ± 0.03	2MASS
W1 [mag]	5.187 ± 0.197	WISE
W2 [mag]	5.097 ± 0.062	WISE
W3 [mag]	5.201 ± 0.014	WISE
T_{eff} [K]	4664 ± 53	ZASPE
$\log g$ [cm s^{-1}]	2.71 ± 0.04	ZASPE + Gaia
[Fe/H] [dex]	-0.19 ± 0.06	ZASPE
$v \sin i$ [km s^{-1}]	2.5 ± 0.3	ZASPE
R_{\star} [R_{\odot}]	9.07 ± 0.63	ZASPE + Gaia
	9.07 ± 0.63	Asteroseis. + TESS
L_{\star} [L_{\odot}]	$29.5^{+1.3}_{-1.0}$	ZASPE + Gaia
M_{\star} [M_{\odot}]	1.0 ± 0.2	PARSEC
	1.29 ± 0.17	Asteroseis. + TESS

Ensemble sampler (Goodman & Weare, 2010), to obtain the best-fit parameters. We used logarithmic priors for P , T_0 , and K , i.e. we fit in terms of $\log P$, $\log T_0$, and $\log K$, and used uniform priors for all other parameters¹. We deployed 32 walkers and ran 3 000 steps for the first burn-in phase until the walkers had explored the parameter space sufficiently. At the end of the first burn-in phase, walkers are re-sampled around the most probable position to reject bad samplings. We then continued with a second burn-in phase for another 3 000 steps. All parameters have clearly converged after the second burn-in phase. Finally, we collected the samples from the last 10 000 steps to calculate the maximum-likelihood set of parameters and estimate the uncertainties. The random zero-point offsets between the different instrumental setups were included as additional free parameters in the fitting process. For consistency with the work of Wittenmyer et al. (2017b), we also added 7 m s^{-1} of stellar jitter in quadrature to the error bars, as is appropriate for this type of star (Kjeldsen & Bedding, 1995),

¹For T_0 , which is technically allowed to assume negative values, this choice of parameterization introduces an unintentional, but weak informative prior on the parameter. However, as the occurrence of T_0 is periodic in uniform space, if fitted with a uniform prior, the posterior distribution may look bi-modal if the initial value is not optimal. Having a logarithmic prior makes the walkers converge to the optimal value quickly, as a linear change in $\log(T_0)$ results in an exponential change in T_0 . Because T_0 is periodic, one positive solution is enough to derive all other solutions.

and as explained in Wittenmyer et al. (2016). Finally, following the method described by (Baluev, 2009), we also included an “instrumental jitter” term in the fitting, which acts to ensure that the uncertainties from the different instrumental setups do not introduce a spurious weighting of the RV points. This can happen if the internal error bars are overestimated or underestimated for some instruments. In our case the internal error bars of the AAT and FIDEOS data seem to be substantially underestimated as indicated by the large positive values of the square of their instrumental jitter terms in Table 2, whereas the MJ1 error bars seem to be somewhat overestimated as indicated by the negative value of the square of their instrumental jitter term in Table 2. The total uncertainty for each RV measurement is thus given by

$$\sigma = \sqrt{\sigma_{\text{int}}^2 + \sigma_{\text{st.jitt.}}^2 + \sigma_{\text{inst.jitt.}}^2} \quad , \quad (1)$$

where σ_{int} is the internal error as reported in Table 5, $\sigma_{\text{st.jitt.}}$ is the stellar jitter, and $\sigma_{\text{inst.jitt.}}$ is the instrumental jitter. The RMS around the combined fit is 14.1 m s^{-1} , and the weighted RMS is 11.7 m s^{-1} . Figure 3 shows all data points together with our best-fit orbital solution, Fig. 4 shows a phase-folded version of that plot, and Fig. 5 shows a close-up view of the RV peak near periastron passage (again phase-folded with the orbital period). A corner plot of the posterior probability distributions of the parameters, generated from the last 10 000 steps and demonstrating that all parameters are well constrained, is shown in Fig. 12 in the appendix.

In order to confirm our MCMC results, we also fitted a single Keplerian orbit using the IDL package RVLIN (Wright & Howard, 2009). Here we estimated the corresponding uncertainties in the orbital parameters via the bootstrapping algorithm from the BOOTTRAN package (Wang et al., 2012) using 100 000 steps. Because the extra instrumental jitter term cannot be set as a free parameter, we used the modified error bars given by Eq. 1 as input to the fitting. While the uncertainty estimates derived with the bootstrapping method are somewhat larger, the two sets of best-fit parameters are in good agreement. Both best-fit single-Keplerian orbital solutions and the corresponding parameter uncertainty estimates are summarized in Table 2.

For the calculation of the semi-major axis and minimum mass of the planet we give the values using both the spectroscopic stellar mass of $M_* = 1.0 \pm 0.2 M_{\odot}$ (see Sect. 4.1), as well as the asteroseismic mass of $1.29 \pm 0.17 M_{\odot}$ (see Sect. 4.2). For the rest of this work we will adopt the spectroscopically derived stellar mass and radius unless otherwise mentioned. Note that the uncertainty in the semi-major axis is completely dominated by the uncertainty in stellar mass, which to a lesser extent also affects the uncertainty in the minimum mass of the planet. Note that Wittenmyer et al. (2017b) used a mass of $1.17 \pm 0.20 M_{\odot}$, which has a comparable

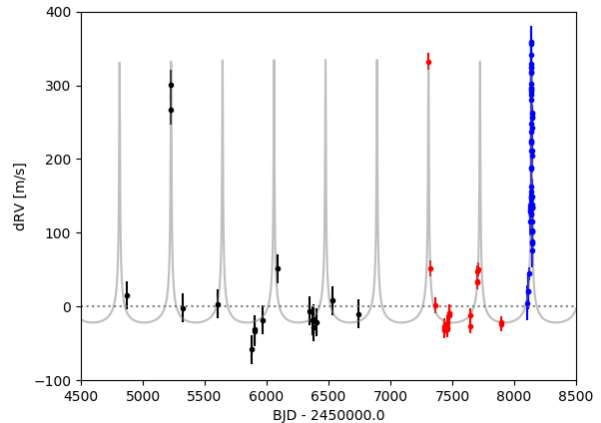


Figure 3. All available RV data together with our best-fit Keplerian orbital solution for HD 76920 b. The black points are the AAT data from Wittenmyer et al. (2017b), the red points are the re-reduced CHIRON and FEROS data, and the blue points are the CHIRON, FEROS, FIDEOS, and HERCULES data taken for this work. Error bars represent the total uncertainty given by Eq. 1. The RMS about this fit is 14.1 m s^{-1} .

relative error. This leads us to believe that their uncertainty estimate for $m_P \sin i$ is underestimated and may not include the uncertainty in stellar mass.

We also searched for periodic signals in the residuals (Fig. 6), but did not find any significant power, as can be seen in the GLS periodogram shown in Fig. 7.

6 COMPANION UPPER MASS LIMIT

6.1 Astrometric limit

To better constrain the mass of HD 76920 b we applied the method presented in Jones et al. (2017) (which is based on Sahlmann et al. 2011), to derive the orbital inclination angle, and thus its dynamical mass. To do this, we combined the orbital elements derived here with the Hipparcos intermediate astrometric data (HIAD) obtained in van Leeuwen (2007b). This dataset comprises a total of 106 one-dimensional abscissa measurements (see section 2.2.2 in van Leeuwen (2007a)), with a mean uncertainty of 1.9 mas. For this purpose, we first attempted to directly obtain a full 7-parameter orbital solution, solving for the inclination angle i and the longitude of the ascending node Ω , while keeping fixed the five parameters derived from the Keplerian fit (P , e , ω , K , T_0), and correcting for the 5 single-star parameters solution (α^* , δ , μ_{α^*} , μ_{δ} , ϖ). Unfortunately, due to the small astrometric signal, in part due to the relatively small parallax (correspondingly large distance) of HD 76920 ($\varpi = 5.41 \pm 0.03 \text{ mas}$; Gaia Collaboration et al. (2018)), and also because of the high eccentricity (a significant astrometric perturbation occurs only close to periastron passage), no significant solution was obtained.

Table 2 Best-fit orbital solution and derived quantities for HD 76920 b.

† A negative value for the square of the instrumental jitter indicates that the formal internal errors are overestimated and that the fitted instrumental jitter needs to be subtracted in quadrature in Eq. 1.

Element	emcee	RVLIN	W17
P [d]	$415.891^{+0.043}_{-0.039}$	415.886 ± 0.047	415.4 ± 0.2
T_0 [BJD - 2450000.0]	$4812.47^{+0.30}_{-0.33}$	4812.52 ± 0.36	4813.42 ± 0.24
e	0.8782 ± 0.0025	0.8847 ± 0.0028	0.856 ± 0.009
ω [°]	1.2 ± 1.0	1.6 ± 1.2	$352.9^{+1.9}_{-1.1}$
K [m s ⁻¹]	$178.1^{+2.7}_{-2.6}$	181.1 ± 3.7	186.8 ± 7.0
a [AU] (spec)	$1.091^{+0.068}_{-0.077}$	1.090 ± 0.103	1.149 ± 0.017
$m_P \sin i$ [M _J] (spec)	$3.13^{+0.41}_{-0.43}$	3.11 ± 0.42	$3.93^{+0.14}_{-0.15}$
a [AU] (seis)	$1.187^{+0.050}_{-0.054}$	1.187 ± 0.074	—
$m_P \sin i$ [M _J] (seis)	$3.71^{+0.32}_{-0.33}$	3.68 ± 0.33	—
RMS about fit [m s ⁻¹]	14.11	13.79	9.74
weighted RMS about fit [m s ⁻¹]	11.71	11.26	—
zero point (AAT) [m s ⁻¹]	$3.1^{+2.7}_{-2.5}$	2.5 ± 4.4	—
zero point (CHIRON) [m s ⁻¹]	$-68.4^{+1.9}_{-2.0}$	-74.2 ± 5.5	—
zero point (FEROS) [m s ⁻¹]	-13.0 ± 3.0	-18.8 ± 5.4	—
zero point (FIDEOS) [m s ⁻¹]	$-93.9^{+4.3}_{-4.0}$	-94.1 ± 7.3	—
zero point (MJ1) [m s ⁻¹]	$-33.6^{+6.0}_{-4.6}$	-37.5 ± 7.0	—
zero point (MJ3) [m s ⁻¹]	$-54.3^{+4.9}_{-5.2}$	-61.6 ± 8.1	—
$\sigma_{inst.jitt.}^2$ (AAT) [m ² s ⁻²]	$324.8^{+128.7}_{-89.2}$	—	—
$\sigma_{inst.jitt.}^2$ (CHIRON) [m ² s ⁻²]	$56.9^{+36.5}_{-26.9}$	—	—
$\sigma_{inst.jitt.}^2$ (FEROS) [m ² s ⁻²]	$14.6^{+43.8}_{-25.8}$	—	—
$\sigma_{inst.jitt.}^2$ (FIDEOS) [m ² s ⁻²]	$473.0^{+186.7}_{-132.3}$	—	—
$\sigma_{inst.jitt.}^2$ (MJ1) [m ² s ⁻²] [†]	$-225.7^{+34.7}_{-22.7}$	—	—
$\sigma_{inst.jitt.}^2$ (MJ3) [m ² s ⁻²]	$153.2^{+110.7}_{-81.7}$	—	—

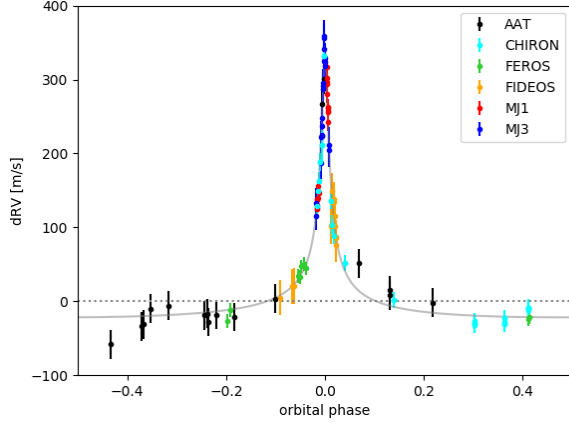


Figure 4. Same as Fig. 3, but phase-folded on the orbital period. Data from different instruments/setups are shown in different colours: AAT — black, CHIRON — cyan, FEROS — green, FIDEOS — orange, MJ1 — red, MJ3 — blue.

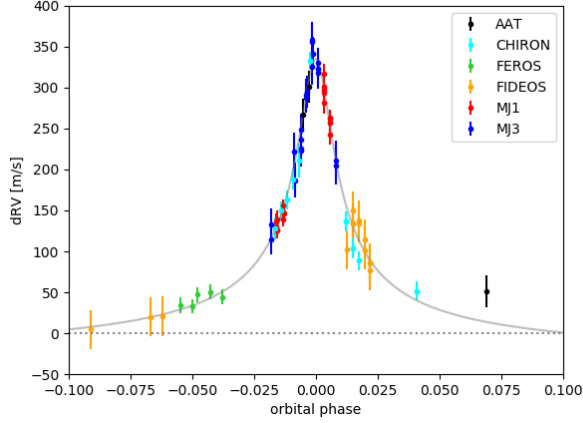


Figure 5. Close-up view of the RV peak near periastron passage. Colour-coding is the same as in Fig. 4.

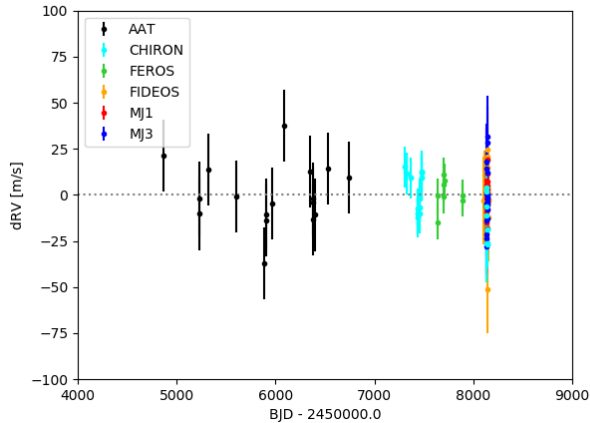


Figure 6. Residuals from the best-fit orbital solution. Error bars represent the total uncertainty given by Eq. 1. Colour-coding is the same as in Fig. 4 and Fig. 5.

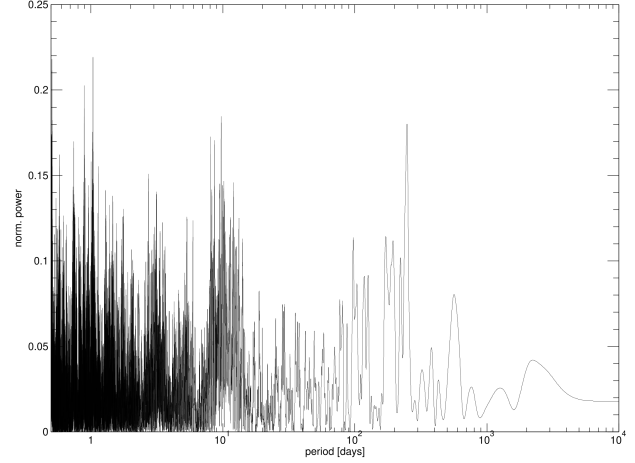


Figure 7. GLS periodogram of the residuals from the best-fit orbital solution shown in Fig. 6.

This basically means that the orbital solution does not improve the standard Hipparcos 5-parameter solution. However, we could still compute an upper mass limit for the companion by injecting synthetic astrometric signals induced by the companion at different inclination angles (the smaller the value of i , the larger the astrometric signal). Briefly, we generated synthetic datasets, keeping fixed the time of the individual epochs of the HIAD and computing the expected astrometric signal induced by the companion by propagating the orbital solution to the epoch of the HIAD observations. This was performed at decreasing inclination angles, while randomly selecting Ω in the range between 0 – 360° . For each synthetic dataset we added Gaussian distributed uncertainties with standard deviation equal to the median abscissa error (1.9 mas in this case). Then we solved the 7-parameter solution to the synthetic datasets until we recovered the simulated (i, Ω) pairs. Figure 8 shows the resulting (i, Ω) values for a total of 100 synthetic datasets, with an input inclination angle of 0.6° , which corresponds to an angular semi-major axis of 1.9 mas. As can be seen, for such a low i -value we are capable of recovering most of the synthetic signals with relatively good accuracy. We obtained a median of $i = 0.54^\circ$ with a standard deviation of 0.37° . We also note that only in eight cases we obtained a reduced χ^2 -value larger than for the Hipparcos 5-parameter solution. For comparison, we repeated this analysis for an inclination angle of 0.8° (corresponding to $a = 1.5$ mas). We obtained a standard deviation of 0.73° , and already in 17% of the simulations the reduced χ^2 of the synthetic solution is larger than for the Hipparcos 5-parameter solution, showing how rapidly the detectability drops with the astrometric amplitude. In fact, only at inclination values of $i < 0.3^\circ$ we obtained reduced χ^2 -values of the synthetic solution lower than for the Hipparcos 5-parameter model in $> 99\%$ of the cases. Based on this analysis, we might adopt a lower

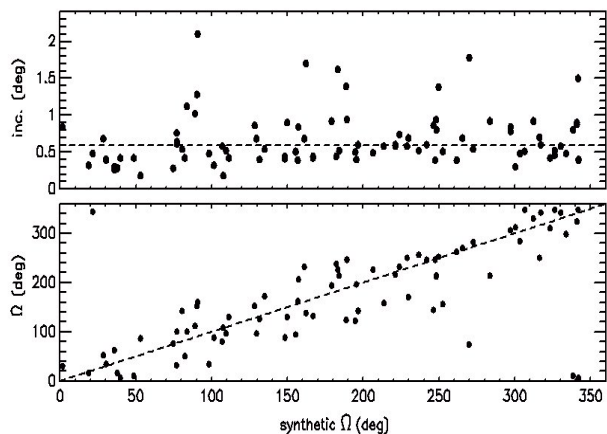


Figure 8. *Upper panel:* Inclination angles recovered from the 100 simulations, as a function of synthetic Ω values. The horizontal dashed line corresponds to the input value of $i = 0.6$ deg. *Lower panel:* Same as the upper panel, but this time for the Ω values. The dashed line corresponds to the one-to-one correlation.

i -value of ~ 0.4 – 0.6° , which corresponds to an upper mass limit for HD 76920 b of ~ 0.4 – $0.6 M_\odot$. Finally, we note that by considering an orbital inclination angle of 90° (edge-on orbit), the astrometric semi-major axis is only $20 \mu\text{as}$, which is comparable to the Gaia precision (Gaia Collaboration et al., 2016). It would thus be very challenging to significantly detect such a small signal even in the Gaia data.

6.2 Geometric limit

The method described in Section 6.1 does not place very stringent upper limits on the mass of the planet. It is therefore interesting to note that we can put a much lower limit on the planet’s mass from simple geometry. While the inclination is unknown, we know that there is no preferred orientation of the orbital plane with respect to the line of sight, in other words the inclination has an isotropic probability density function (pdf). This corresponds to a pdf that is flat in $\cos i$, which makes it easy to draw from for a Monte Carlo simulation using random inclination angles. We used a sample size of 10^8 and found a $3\text{-}\sigma$ (99.73% confidence) upper mass limit of $42.6 M_J$, corresponding to an inclination of 4.2° . Results for a number of confidence levels are summarized in Table 3.

7 SUMMARY AND DISCUSSION

We obtained 63 new radial velocity measurements of HD 76920 from four different instruments around the time of the predicted periastron passage. The unusually high eccentricity of HD 76920 b means that $\sim 90\%$ of the peak-to-peak RV is traversed up and down in only $\sim 14\%$

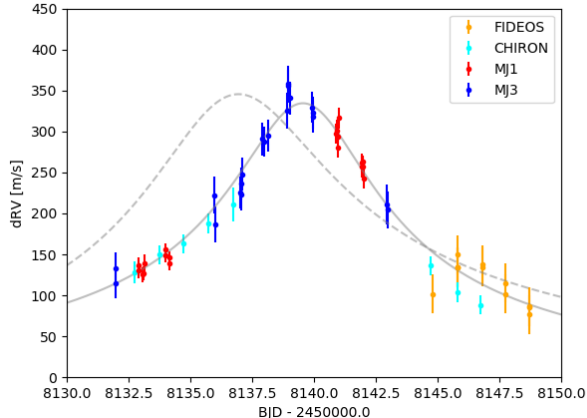
of the orbital period, and the RV curve is approximately flat for the remaining ~ 360 days of the orbital period, making it difficult to determine precise orbital elements from an observational point of view. However, in order to constrain the orbital elements, it is essential to have good sampling of the non-flat parts of the orbit where the RV changes rapidly over time. As the orbital phase near periastron passage was not very well covered in their initial work, Wittenmyer et al. (2017b) suggested follow-up observations be carried out during the next periastron passage. Flexible scheduling of observing time during periastron passage on telescopes with high-resolution spectrographs is an effective way of confirming the nature of highly eccentric planets and determining their orbital properties and minimum mass to high precision. For example, HD 37605 b with an eccentricity of $e = 0.74$, or HD 45350 b with an eccentricity of $e = 0.76$ have been confirmed in this way (Cochran et al., 2004; Endl et al., 2006).

We were fortunate enough to be granted access to the HERCULES, CHIRON, FEROS, and FIDEOS spectrographs during that period, and hence managed to obtain near-continuous coverage of the corresponding RV peak. In hindsight, getting enough telescope time either side of the predicted periastron passage was particularly important because the periastron passage actually happened about 3 days later than predicted, or about 3.7-sigma when we calculate the uncertainty on the time of periastron passage via bootstrapping based on the orbital elements given by Wittenmyer et al. (2017b) (see Fig. 9). This highlights the importance and scientific value of small-to-medium size telescopes with high-resolution spectrographs to the exoplanet community (e.g. Swift et al., 2015; Addison et al., 2019), as it would have been near impossible to get enough time on larger telescopes at such short notice.

Our best-fit orbital solution to the combined data set from a total of five instruments (and six different operating modes) yielded an even higher than expected eccentricity of $e = 0.88$ and an orbital period of 415.9 d. We also found a RV semi-amplitude of 178 m s^{-1} , and a semi-major axis of 1.09 AU. The new orbital solution corresponds to minimum mass of $3.1 M_J$ for the planet that is about 20% lower than that reported by Wittenmyer et al. (2017b), mainly owing to our new lower stellar mass estimate. Formally, the RMS of the residuals from our fit is larger than in Wittenmyer et al. (2017b), partly because the individual uncertainties in and the scatter of the HERCULES data are about three times larger compared to the other instruments, and partly because we have effectively given different weights to the RV measurements during the fitting via the error treatment described in section 5. In particular, note that the RMS of the AAT residuals from our best fit is now 17.0 m s^{-1} , which is of course expected as they now carry less weight compared to (Wittenmyer et al., 2017b). More impor-

Table 3 Geometric upper mass limits and corresponding inclinations for HD 76920 b for different confidence levels.

confidence level	upper mass limit [M_J]	inclination [$^\circ$]
99.73%	42.6	4.2
99%	22.2	8.1
95%	10.0	18.2
90%	7.2	25.8

**Figure 9.** Comparison of the best-fit model RV curve from this work (solid grey line) with the one from Wittenmyer et al. (2017b) (dashed grey line). The periastron passage happened about 3 days later than predicted by the orbital elements from Wittenmyer et al. (2017b).

tantly though, due to the much improved phase coverage near periastron passage the uncertainties in the orbital elements are now significantly reduced. Notably, the uncertainty in the orbital period was reduced by a factor of 5, and the uncertainty in the eccentricity was reduced by more than a factor of 3. In addition, we also estimated an upper mass limit of $0.4\text{--}0.6 M_\odot$ for the companion from HIPPARCOS astrometry, and a $3\text{-}\sigma$ upper mass limit of $42.6 M_J$ from geometric considerations.

7.1 Star–Planet Interactions

Note that our value of the semi-major axis is slightly smaller the one given by Wittenmyer et al. (2017b), while our eccentricity is slightly larger. However, this seemingly small difference means that the planet actually comes to within 2.4 ± 0.3 stellar radii from its host star’s surface at closest approach, or about one stellar radius closer than estimated by Wittenmyer et al. (2017b). Also note that we calculate the same value for planet’s distance from the stellar surface at periastron in units of the stellar radius, independent of whether we use the spectroscopic or the asteroseismic stellar parameters. Naturally, this makes the system a prime target for studies of star–planet interactions.

The orbital evolution is determined by the combined

effect of tidally induced orbital decay and mass-loss induced orbital expansion. Following the same procedure as in Villaver et al. (2014) and Wittenmyer et al. (2017b), we determined the planet’s orbit and eccentricity evolution as the star evolves up the Red Giant Branch, and the tidal dissipation is dominated by motions in the star’s convective envelope (Zahn, 1977). We have updated both the planetary and stellar parameters since Wittenmyer et al. (2017b). We use SSE stellar models (Hurley et al., 2000) with the asteroseismic mass of $1.3 M_\odot$ and a Solar metallicity. We furthermore consider two values for the Reimers η mass loss parameter (Reimers, 1975): a standard value of $\eta = 0.6$, and an extreme case of $\eta = 0.0$ (no mass loss). The latter means that the planet experiences only tidal decay on its orbit, not any orbital expansion owing to mass loss, and hence represents an optimal case for a maximum orbital decay owing to tidal forces.

In each case, the planet’s orbit undergoes only very minor decay before the planet is engulfed in the stellar envelope: for both $\eta = 0.6$ and $\eta = 0.0$, the orbital eccentricity decays by only about 0.002 before the star engulfs the planet. With no stellar mass loss ($\eta = 0.0$), the semi-major axis decays by 0.01 AU, while with mass loss ($\eta = 0.6$) the semi-major axis increases by 0.003 AU. The planet enters the stellar envelope when the star has grown to a little over 3 times its present radius, some 50 Myr hence. Adopting the spectroscopic stellar mass of $1.0 M_\odot$ does not qualitatively change the future evolution: the eccentricity decay is a little larger (0.004 – 0.005) and the remaining lifetime a little longer (~ 80 Myr), but there are still no large changes to the orbit expected.

7.2 Transit Probability

Our updated orbital solution also leads to an even higher transit probability than the 10.3% reported in Wittenmyer et al. (2017b). From the `emcee` best-fit orbital elements listed in Table 2, it follows that at inferior conjunction, which happens at a true anomaly of 88.8° and 5.06 d after periastron passage, the star–planet separation is 0.245 AU, and the azimuthal component of the orbital velocity is 60.7 km s^{-1} . In order to calculate the probability, depth, and duration of a potential transit, we must first have an estimate of the planetary radius. We used the mass–radius relationship for the Jovian regime in form of the power law $R_{pl} \propto m_p^{-0.04}$

as given by (Chen & Kipping, 2017), with which we calculated the planet’s radius to be $0.96 R_J$. With that in hand, we calculated a relatively high transit probability of 16.0%, using Eq. 5 from Kane & von Braun (2008), with a duration of 2.2 d and a transit depth of 0.013% or 130 ppm, assuming an inclination of $i = 90^\circ$ and ignoring limb darkening effects. While the large stellar radius increases the transit probability, unfortunately it also decreases the transit depth, requiring a level of photometric precision that is extremely challenging for ground-based transit searches, albeit perhaps not impossible (e.g. Tregloan-Reed & Southworth, 2013). However, TESS can technically achieve the required precision for a star of this magnitude (Ricker et al., 2015). HD 76920 has ecliptic coordinates of about $\lambda = 202.5^\circ$ and $\beta = -73.2^\circ$, and therefore lies about five degrees outside the southern TESS continuous viewing zone. However, by pure coincidence, this placed HD 76920 inside the sector that TESS was observing at the time of the next potential transit (sector 9), which we predicted to occur approximately between $JD2458559.43 \pm 0.63$ and $JD2458561.66 \pm 0.63$ (UT 16.93–19.16 March 2019). We list predicted mid-transit times, as well as ingress and egress times for potential future transits in Table 4.

Unfortunately, due to it being an evolved star, HD 76920 presents a photometric variability at the 500 ppm level, which is significantly larger than the expected transit depth. However, before searching for a potential transit signal, we corrected the light curve using a Gaussian process (GP), following a similar procedure to that described in Jones et al. (2019). The fit was performed with the *Juliet* code (Espinoza et al., 2019) using a Matérn kernel. To model the asteroseismic signal we used a Gaussian prior with mean equal to the period corresponding to ν_{max} , as derived in section 4.2. Figure 10 shows the TESS light curve and the GP model.

Finally, to determine if the planet transits on the predicted date, we compared the Bayesian evidence between a transit model and a non-transit model. As we found no significant difference, we assumed the simpler model, i.e. the non-transit model. The GP corrected light curve around the expected transit time is shown in Figure 11.

7.3 Origin of the high eccentricity

The origin of Hot Jupiters and/or highly eccentric planets is usually explained via the Kozai-Lidov mechanism, whereby perturbations caused by a massive third body (i.e. a stellar companion) can cause oscillations between the planet’s eccentricity and inclination as long as its angular momentum component parallel to the orbital angular momentum of the two stars remains constant (Lidov, 1962; Kozai, 1962). However, as already noted by Wittenmyer et al. (2017b), there are no indications for additional massive companions in the RV data. Also, while the Gaia DR2 catalogue (Gaia Collab-

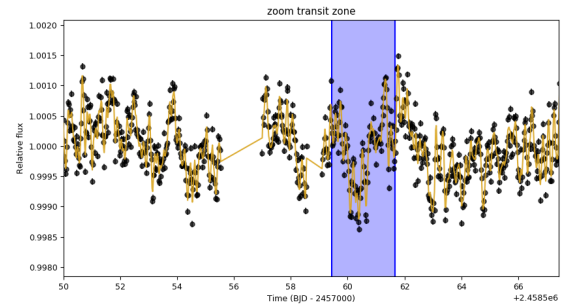


Figure 10. TESS light curve around the expected transit time, which is highlighted in light blue. The yellow line represents the Gaussian process fit.

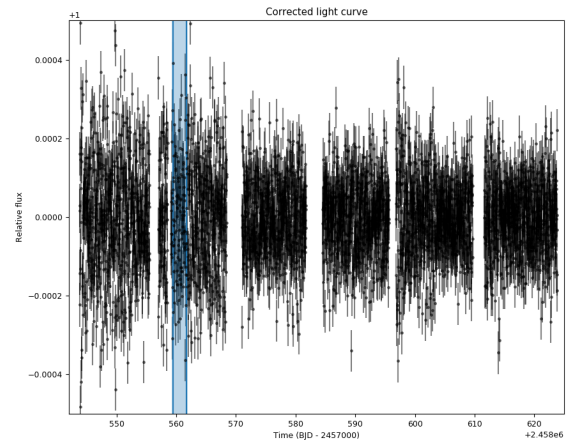


Figure 11. GP corrected TESS light curve of HD 76920. The expected transit time is highlighted in light blue.

oration et al., 2016, 2018) lists two faint ($G \sim 21$ mag) stellar objects (Gaia DR2 IDs 5224124753994137984 and 5224127812011479808) with compatible parallaxes within 5 arcmins from HD 76920, corresponding to a physical separation of $\lesssim 55\,000$ AU at a distance of $d = 184$ pc (Bailer-Jones et al., 2018), their respective proper motions and $B - R$ colours are very different from the corresponding values for HD 76920, which rules them out as physically close companions. Furthermore, as also noted by Wittenmyer et al. (2017b), in the Kozai-Lidov scenario planets like HD 76920 b are readily being engulfed by their host stars as they move up the red giant branch (Frewen & Hansen, 2016), and, according to simulations by Parker et al. (2017), free-floating planets are almost exclusively captured into much wider orbits ($a > 100$ AU). This leaves planet-planet scattering as the most likely explanation for the highly eccentric orbit of HD 76920 b (e.g. Chatterjee et al., 2008). In this scenario, a second planet of comparable mass would have either been ejected from the system as the result of a close encounter with HD 76920 b, or at least pushed

Table 4 Predicted windows for potential past and future transits of HD 76920 b.

ingress	mid-transit [JD - 2400000.0]	egress	UT date (mid)
58559.43 ± 0.63	58560.55 ± 0.54	58561.66 ± 0.63	18 Mar 2019
58975.32 ± 0.66	58976.44 ± 0.58	58977.56 ± 0.66	06 May 2020
59391.21 ± 0.68	59392.33 ± 0.61	59393.45 ± 0.68	26 Jun 2021
59807.10 ± 0.71	59808.22 ± 0.64	59809.34 ± 0.71	16 Aug 2022
60222.99 ± 0.75	60224.11 ± 0.68	60225.23 ± 0.75	06 Oct 2023

outwards into a long-period orbit that is beyond our current detection limits. A third option is that the second planet disappeared from the system because it was thrown towards the star and engulfed by it.

7.4 Additional Considerations

The very high eccentricity of HD 76920 b not only makes it the most eccentric planet known to orbit an evolved star by some margin, but also puts it in fifth place amongst all known exoplanets². Its eccentricity is only surpassed by HD 4113 A b ($e = 0.90$) (Tamuz et al., 2008), HD 7449 A b ($e = 0.92$) (Dumusque et al., 2011; Wittenmyer et al., 2019a), HD 80606 b ($e = 0.93$) (Naef et al., 2001; Moutou et al., 2009), and HD 20782 b ($e = 0.97$) (Jones et al., 2006; O’Toole et al., 2009; Kane et al., 2016), all of which are gas giants orbiting solar-mass main-sequence stars.

Several studies have highlighted the possibility that a RV curve produced by two low-eccentricity planets can be misinterpreted as being caused by one planet with medium to high eccentricity, especially for low signal-to-noise ratios K/σ , poor sampling, and/or if the two planets are in resonant orbits (e.g. Shen & Turner, 2008; Rodigas & Hinz, 2009; Anglada-Escudé et al., 2010; Wittenmyer et al., 2012, 2013, 2019a,b). However, given the large K/σ ratio, the dense sampling we have achieved around periastron passage, and the very high eccentricity (which is well outside the "danger zone" as identified by Wittenmyer et al. (2019b), i.e. the range of eccentricities that can be most easily mimicked by two near-circular planets), we are very confident that the results presented in this paper remove any possibly remaining doubts about the RV variations being caused by a single planetary companion in a highly eccentric orbit.

8 ACKNOWLEDGEMENTS

CB was supported by Australian Research Council Discovery Grant DP170103491. LV acknowledges support from

CONICYT through projects Fondecyt n. 1171364 and Anillo ACT-1417. AZ is supported by CONICYT grant n. 2117053. SW thanks the Heising-Simons Foundation for their generous support. AJM acknowledges support from the Knut and Alice Wallenberg Foundation (project grant 2014.0017), the Swedish Research Council (starting grant 2017-04945), and the Walter Gyllenberg Foundation of the Royal Physiographic Society of Lund. RB acknowledges support from FONDECYT Project 11200751, from CORFO project N°14ENI2-26865, and from project IC120009 “Millennium Institute of Astrophysics (MAS)” of the Millenium Science Initiative, Chilean Ministry of Economy. We are grateful for receiving a generous allocation of observing time at UCMJO. This research has made use of NASA’s Astrophysics Data System (ADS), and the SIMBAD database, operated at CDS, Strasbourg, France. This research has also made use of the Extrasolar Planets Encyclopaedia at <http://www.exoplanet.eu>. This work has made use of data from the European Space Agency (ESA) mission *Gaia* (<https://www.cosmos.esa.int/gaia>), processed by the *Gaia* Data Processing and Analysis Consortium (DPAC, <https://www.cosmos.esa.int/web/gaia/dpac/consortium>). Funding for the DPAC has been provided by national institutions, in particular the institutions participating in the *Gaia* Multilateral Agreement. Finally, we would like to thank the anonymous referee for their insightful comments that helped noticeably to improve this manuscript.

A RADIAL VELOCITY DATA

B CORNER PLOT OF THE FIT PARAMETERS

REFERENCES

- Adamów M., Niedzielski A., Villaver E., Nowak G., Wolszczan A., 2012, *ApJ*, 754, L15
- Adamów M., Niedzielski A., Kowalik K., Villaver E., Wolszczan A., Maciejewski G., Gromadzki M., 2018, *A&A*, 613, A47
- Addison B., et al., 2019, *PASP*, 131, 115003
- Anglada-Escudé G., López-Morales M., Chambers J. E., 2010, *ApJ*, 709, 168
- Bailer-Jones C. A. L., Rybizki J., Fouesneau M., Man-telet G., Andrae R., 2018, *AJ*, 156, 58

²<http://exoplanet.eu> (Schneider et al., 2011). Note that when last accessed on 31 January 2021, WASP-74 b was erroneously listed to have an eccentricity of 0.88, but it really is the limb-darkening coefficient ϵ that has this value (Luque et al., 2020).

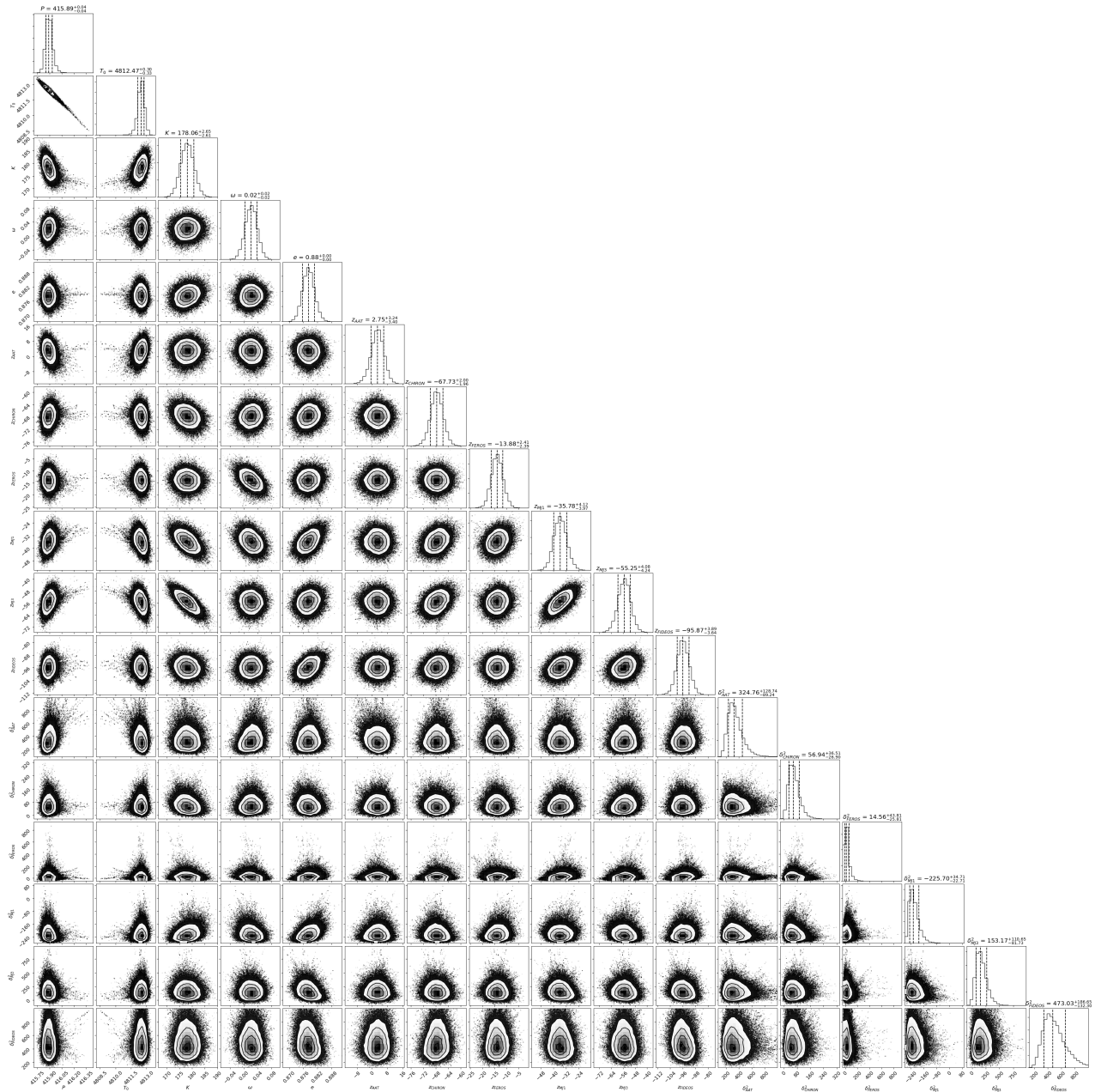


Figure 12. Corner plot of the posterior probability distributions of the 17 free parameters used in the emcee fitting. All numerical values shown are rounded to two decimal places.

Table 5 Radial velocities for HD 76920. Note that the velocities shown have instrument-specific zero points, which are included in the fitting process and are given in Table 2. The AAT data was taken from Wittenmyer et al. (2017b).

BJD-2450000.0	RV [m s ⁻¹]	$\sigma_{RV,int}$ [m s ⁻¹]	Instr.	BJD - 2450000.0	RV [m s ⁻¹]	$\sigma_{RV,int}$ [m s ⁻¹]	Instrument
				8101.764230	-91.1	6.4	FIDEOS
				8111.810817	-75.7	5.9	FIDEOS
				8113.812973	-74.9	7.6	FIDEOS
				8144.796552	6.0	7.2	FIDEOS
				8145.804861	38.7	6.9	FIDEOS
				8145.811483	38.0	6.8	FIDEOS
				8145.818042	38.2	7.3	FIDEOS
				8145.825082	53.7	7.1	FIDEOS
				8146.795174	38.5	6.3	FIDEOS
				8146.802702	42.0	6.2	FIDEOS
				8147.748904	5.8	6.4	FIDEOS
				8147.756478	19.0	6.6	FIDEOS
				8148.710383	-9.9	6.6	FIDEOS
				8148.718152	-9.4	6.2	FIDEOS
				8148.725379	-19.2	7.3	FIDEOS
				8132.894243	101.3	16.4	MJ1
				8132.916154	94.8	16.6	MJ1
				8133.082251	89.7	16.1	MJ1
				8133.104068	91.0	15.6	MJ1
				8133.129350	103.0	17.4	MJ1
				8133.985792	112.8	15.5	MJ1
				8134.008329	119.8	15.5	MJ1
				8134.142827	103.6	15.7	MJ1
				8134.165035	110.1	15.7	MJ1
				8140.904009	261.4	18.3	MJ1
				8140.926304	265.6	18.4	MJ1
				8140.948490	245.1	18.3	MJ1
				8140.970459	257.5	19.7	MJ1
				8140.993368	280.5	18.4	MJ1
				8141.920501	226.1	17.5	MJ1
				8141.940818	220.8	18.9	MJ1
				8141.968963	221.5	18.3	MJ1
				8141.990759	226.9	15.7	MJ1
				8142.013180	206.3	17.4	MJ1
				8131.973084	77.4	14.4	MJ3
				8131.995427	59.8	12.4	MJ3
				8135.979715	166.9	17.1	MJ3
				8136.002019	131.8	16.6	MJ3
				8137.019531	170.2	13.7	MJ3
				8137.041852	181.2	13.3	MJ3
				8137.064108	168.3	13.8	MJ3
				8137.089041	192.7	14.5	MJ3
				8137.919896	235.7	14.3	MJ3
				8137.974526	232.1	11.8	MJ3
				8138.133998	240.0	13.5	MJ3
				8138.922459	269.9	16.4	MJ3
				8138.944974	303.4	16.7	MJ3
				8138.969931	300.3	14.2	MJ3
				8139.032653	285.9	14.2	MJ3
				8139.912303	274.3	12.9	MJ3
				8139.944173	268.1	13.2	MJ3
				8139.966157	262.9	13.5	MJ3
				8142.931486	155.6	20.3	MJ3
				8142.975638	149.0	17.9	MJ3
4867.07428	17.9	2.2	AAT				
5226.21880	269.5	5.3	AAT				
5227.20104	303.4	3.7	AAT				
5318.89227	1.0	1.9	AAT				
5602.04422	6.1	1.9	AAT				
5880.22005	-55.3	2.3	AAT				
5906.11204	-31.3	1.8	AAT				
5907.19640	-28.1	2.6	AAT				
5969.07596	-15.5	2.1	AAT				
6088.86366	54.1	3.8	AAT				
6344.02991	-3.1	2.7	AAT				
6374.98803	-16.4	2.4	AAT				
6376.95955	-14.1	2.4	AAT				
6377.96197	-25.2	2.6	AAT				
6399.96882	-18.5	3.1	AAT				
6530.31941	11.0	3.0	AAT				
6744.98572	-7.3	2.4	AAT				
7306.82769	264.5	4.4	CHIRON				
7324.78909	-16.0	4.5	CHIRON				
7365.78945	-66.0	4.1	CHIRON				
7433.69902	-97.2	3.6	CHIRON				
7433.71312	-99.6	3.4	CHIRON				
7433.72722	-94.7	3.4	CHIRON				
7458.68833	-90.4	3.3	CHIRON				
7458.70243	-95.2	3.7	CHIRON				
7458.71651	-98.4	3.6	CHIRON				
7478.64626	-76.3	4.1	CHIRON				
7478.66036	-79.6	3.7	CHIRON				
7478.67445	-77.2	3.7	CHIRON				
8132.74057	60.5	8.0	CHIRON				
8133.75634	81.7	6.2	CHIRON				
8134.73750	95.1	5.0	CHIRON				
8135.72967	120.3	7.0	CHIRON				
8136.74525	143.4	18.1	CHIRON				
8144.69957	68.5	6.0	CHIRON				
8145.80543	36.0	6.9	CHIRON				
8146.73179	20.7	5.3	CHIRON				
7641.91298	-40.6	4.0	FEROS				
7643.90565	-25.6	5.1	FEROS				
7700.84513	20.7	5.4	FEROS				
7702.87010	19.1	4.3	FEROS				
7703.79908	33.4	4.5	FEROS				
7705.85500	36.7	4.3	FEROS				
7894.56042	-38.1	4.2	FEROS				
7895.46977	-35.7	3.8	FEROS				
8123.84502	30.5	4.1	FEROS				

- Baluev R. V., 2009, *MNRAS*, 393, 969
- Baraffe I., Homeier D., Allard F., Chabrier G., 2015, *A&A*, 577, A42
- Bergmann C., 2015, PhD thesis, University of Canterbury, New Zealand
- Bergmann C., Endl M., Hearnshaw J. B., Wittenmyer R. A., Wright D. J., 2015, *IJAsB*, 14, 173
- Borucki W. J., et al., 2010, *Science*, 327, 977
- Brahm R., Jordán A., Espinoza N., 2017a, *PASP*, 129, 034002
- Brahm R., Jordán A., Hartman J., Bakos G., 2017b, *MNRAS*, 467, 971
- Bressan A., Marigo P., Girardi L., Salasnich B., Dal Cero C., Rubele S., Nanni A., 2012, *MNRAS*, 427, 127
- Butler R. P., Marcy G. W., Williams E., McCarthy C., Dosanjuh P., Vogt S. S., 1996, *PASP*, 108, 500
- Castelli F., Kurucz R. L., 2004, arXiv Astrophysics e-prints,
- Chatterjee S., Ford E. B., Matsumura S., Rasio F. A., 2008, *ApJ*, 686, 580
- Chen J., Kipping D., 2017, *ApJ*, 834, 17
- Cochran W. D., et al., 2004, *ApJ*, 611, L133
- Diego F., Charalambous A., Fish A. C., Walker D. D., 1990, in Crawford D. L., ed., Proc. SPIE Vol. 1235, Instrumentation in Astronomy VII. pp 562–576, doi:10.1117/12.19119
- Dumusque X., et al., 2011, *A&A*, 535, A55
- Endl M., Kürster M., Els S., 2000, *A&A*, 362, 585
- Endl M., Cochran W. D., Wittenmyer R. A., Hatzes A. P., 2006, *AJ*, 131, 3131
- Espinoza N., Kossakowski D., Brahm R., 2019, *MNRAS*, 490, 2262
- Foreman-Mackey D., Hogg D. W., Lang D., Goodman J., 2013, *PASP*, 125, 306
- Frewen S. F. N., Hansen B. M. S., 2016, *MNRAS*, 455, 1538
- Frink S., Mitchell D. S., Quirrenbach A., Fischer D. A., Marcy G. W., Butler R. P., 2002, *ApJ*, 576, 478
- Gaia Collaboration et al., 2016, *A&A*, 595, A1
- Gaia Collaboration et al., 2018, *A&A*, 616, A1
- Galland F., Lagrange A.-M., Udry S., Chelli A., Pepe F., Beuzit J.-L., Mayor M., 2005, *A&A*, 444, L21
- Goodman J., Weare J., 2010, *Communications in Applied Mathematics and Computational Science*, Vol.~5, No.~1, p.~65-80, 2010, 5, 65
- Hearnshaw J. B., Barnes S. I., Kershaw G. M., Frost N., Graham G., Ritchie R., Nankivell G. R., 2002, *Experimental Astronomy*, 13, 59
- Hurley J. R., Pols O. R., Tout C. A., 2000, *MNRAS*, 315, 543
- Johnson J. A., et al., 2007, *ApJ*, 665, 785
- Johnson J. A., Aller K. M., Howard A. W., Crepp J. R., 2010, *PASP*, 122, 905
- Jones H. R. A., Butler R. P., Tinney C. G., Marcy G. W., Carter B. D., Penny A. J., McCarthy C., Bailey J., 2006, *MNRAS*, 369, 249
- Jones M. I., Jenkins J. S., Rojo P., Melo C. H. F., 2011, *A&A*, 536, A71
- Jones M. I., et al., 2016, *A&A*, 590, A38
- Jones M. I., Brahm R., Wittenmyer R. A., Drass H., Jenkins J. S., Melo C. H. F., Vos J., Rojo P., 2017, *A&A*, 602, A58
- Jones M. I., et al., 2018, *A&A*, 613, A76
- Jones M. I., et al., 2019, *A&A*, 625, A16
- Kane S. R., von Braun K., 2008, *ApJ*, 689, 492
- Kane S. R., Reffert S., Henry G. W., Fischer D., Schwab C., Clubb K. I., Bergmann C., 2010, *ApJ*, 720, 1644
- Kane S. R., et al., 2016, *ApJ*, 821, 65
- Kaufer A., Stahl O., Tubbesing S., Nørregaard P., Avila G., Francois P., Pasquini L., Pizzella A., 1999, *The Messenger*, 95, 8
- Kjeldsen H., Bedding T. R., 1995, *A&A*, 293, 87
- Kozai Y., 1962, *AJ*, 67, 591
- Lidov M. L., 1962, *Planet. Space Sci.*, 9, 719
- Luque R., et al., 2020, *A&A*, 642, A50
- Mayor M., Queloz D., 1995, *Nature*, 378, 355
- Moutou C., et al., 2009, *A&A*, 498, L5
- Naef D., et al., 2001, *A&A*, 375, L27
- Niedzielski A., et al., 2007, *ApJ*, 669, 1354
- O’Toole S. J., Tinney C. G., Jones H. R. A., Butler R. P., Marcy G. W., Carter B., Bailey J., 2009, *MNRAS*, 392, 641
- Parker R. J., Lichtenberg T., Quanz S. P., 2017, *MNRAS*, 472, L75
- Quinn S. N., et al., 2015, *ApJ*, 803, 49
- Ramm D. J., et al., 2016, *MNRAS*, 460, 3706
- Reffert S., Bergmann C., Quirrenbach A., Trifonov T., Künstler A., 2015, *A&A*, 574, A116
- Reimers D., 1975, *Memoires of the Societe Royale des Sciences de Liege*, 8, 369
- Ricker G. R., et al., 2015, *Journal of Astronomical Telescopes, Instruments, and Systems*, 1, 014003
- Rodigas T. J., Hinz P. M., 2009, *ApJ*, 702, 716
- Sahlmann J., et al., 2011, *A&A*, 525, A95
- Sato B., et al., 2003, *ApJ*, 597, L157
- Schneider J., Dedieu C., Le Sidaner P., Savalle R., Zolotukhin I., 2011, *A&A*, 532, A79
- Shen Y., Turner E. L., 2008, *ApJ*, 685, 553
- Skuljan J., 2004, in Kurtz D. W., Pollard K. R., eds, *Astronomical Society of the Pacific Conference Series Vol. 310, IAU Colloq. 193: Variable Stars in the Local Group*. p. 575
- Swift J. J., et al., 2015, *Journal of Astronomical Telescopes, Instruments, and Systems*, 1, 027002
- Tamuz O., et al., 2008, *A&A*, 480, L33
- Tokovinin A., Fischer D. A., Bonati M., Giguere M. J.,

- Moore P., Schwab C., Spronck J. F. P., Szymkowiak A., 2013, *PASP*, 125, 1336
- Tonry J., Davis M., 1979, *AJ*, 84, 1511
- Tregloan-Reed J., Southworth J., 2013, *MNRAS*, 431, 966
- Vanzi L., et al., 2018, *MNRAS*, 477, 5041
- Villaver E., Livio M., Mustill A. J., Siess L., 2014, *ApJ*, 794, 3
- Wang Sharon X., et al., 2012, *ApJ*, 761, 46
- Wittenmyer R. A., Endl M., Wang L., Johnson J. A., Tinney C. G., O'Toole S. J., 2011, *ApJ*, 743, 184
- Wittenmyer R. A., et al., 2012, *ApJ*, 753, 169
- Wittenmyer R. A., et al., 2013, *ApJS*, 208, 2
- Wittenmyer R. A., et al., 2016, *ApJ*, 818, 35
- Wittenmyer R. A., Jones M. I., Zhao J., Marshall J. P., Butler R. P., Tinney C. G., Wang L., Johnson J. A., 2017a, *AJ*, 153, 51
- Wittenmyer R. A., et al., 2017b, *AJ*, 154, 274
- Wittenmyer R. A., Clark J. T., Zhao J., Horner J., Wang S., Johns D., 2019a, *MNRAS*, 484, 5859
- Wittenmyer R. A., Bergmann C., Horner J., Clark J., Kane S. R., 2019b, *MNRAS*, 484, 4230
- Wright J. T., Howard A. W., 2009, *ApJS*, 182, 205
- Zahn J. P., 1977, *A&A*, 500, 121
- Zechmeister M., Kürster M., 2009, *A&A*, 496, 577
- van Leeuwen F., ed. 2007a, *Hipparcos, the New Reduction of the Raw Data Astrophysics and Space Science Library Vol. 350*, doi:10.1007/978-1-4020-6342-8.
- van Leeuwen F., 2007b, *A&A*, 474, 653